

Non-classical Temperature Dependence of Chirality-Induced Magnetization and Its Implications for RNA's Homochirality

Yael Kapon^{#1}, Lilach Brann^{#1}, Shira Yochelis¹, Jonas Fransson², Dimitar D. Sasselov³, Yossi Paltiel^{*1}, and S. Furkan Ozturk^{†3, 4}

¹*Department of Applied Physics, The Hebrew University, Jerusalem 9190401, Israel*

²*Department of Physics and Astronomy, Uppsala University, Uppsala 752 36, Sweden*

³*Harvard-Smithsonian Center for Astrophysics, Cambridge, MA 02138, USA*

⁴*King's College, Cambridge, CB2 1ST, UK*

December 10, 2024

Abstract

The single-handedness of biomolecules is a characteristic feature of life on Earth, yet achieving and maintaining a homochiral prebiotic network is a significant challenge. In our previous studies, we reached homochirality in an RNA precursor, ribo-aminooxazoline (RAO), using magnetized magnetite surfaces as chiral reagents, due to the chiral-induced spin selectivity (CISS) effect. We further demonstrated that RAO can induce net magnetization on previously demagnetized surfaces, indicating a self-reinforcing feedback between chiral molecules and magnetic surfaces. However, these processes depend on spin interactions that generally weaken at higher temperatures, raising concerns about the robustness of our mechanisms in natural settings. Additionally, the temperature dependence of CISS remains poorly understood. To address these questions, we investigated the temperature dependence of chirality-induced magnetization. Contrary to classical expectations, we observed a significant increase in induced net magnetization with increasing temperatures, suggesting a phonon-assisted process. Concurrently, we noted a corresponding increase in the relative yield of RAO during its prebiotic synthesis. Our results support a vibronic contribution to CISS and indicate that spin-controlled processes leading to RNA homochirality can occur reliably and effectively over a range of temperatures likely present in prebiotic environments.

Life is intrinsically linked to planetary environments, with prebiotic chemistry constrained by the environmental conditions [1]. These planetary environments present a wide range of conditions that vary over different timescales, from diurnal fluctuations to gradual geological shifts. Consequently, the processes leading to the formation of the first cells must be both robust and adaptable to these dynamic conditions. A critical process in life's origins is the emergence of homochirality, the single-handedness of biomolecules. Establishing homochirality at the monomer level in prebiotic synthesis is likely essential for the emergence of a functional genetic polymer, like RNA, with high yields and selectivity [2, 3]. Nevertheless, despite its significance, achieving and maintaining a homochiral prebiotic network has long been an unresolved problem for prebiotic chemistry [4]. Numerous

*paltiel@mail.huji.ac.il

†sukrufurkanozturk@g.harvard.edu

#These authors contributed equally to this work.

hypotheses have been proposed for chiral symmetry breaking and the amplification of enantiomeric excess [5]. Yet, none of these have demonstrated a robust mechanism for breaking chiral symmetry in a prebiotic molecule and amplifying it to homochirality from fully racemic starting materials, whereby the chiral information can be effectively propagated to establish a homochiral network (Figure 1b).

To address this challenge, we previously demonstrated a prebiotically plausible method to achieve homochirality in ribo-aminooxazoline (RAO), a compound central to cyanosulfidic chemistry—a high-yielding prebiotic network discovered by the Sutherland group—and to the synthesis of RNA and DNA [6–8]. We obtained RAO in its homochiral form by crystallizing it from a racemic solution of pentose aminooxazolines on a magnetized magnetite (Fe_3O_4) surface, through a process governed entirely by the physical environment [9] (Figure 1b). In subsequent work, we confirmed the reciprocal nature of this effect by showing that RAO molecules can induce an avalanche magnetization in magnetite, indicating a cooperative feedback between chiral molecules and magnetic surfaces in early Earth environments [10, 11] (Figure 1a). Based on empirical evidence, we then proposed a pathway by which homochirality achieved in a single chiral compound, RAO, can effectively propagate throughout the prebiotic network, beginning with *D*-nucleic acids, propagating to *L*-peptides through coded peptide synthesis [12, 13], and eventually leading to homochiral metabolites, thereby accounting for life’s homochirality at the network level [14]. Our previous findings suggest that evaporative lakes with authigenic magnetite sediments [15], which are magnetized under a planetary magnetic field with a hemispherical scale of uniformity, can accommodate enantioselective processes controlled by electron spin [3, 16].

Central to our findings is the chiral-induced spin selectivity (CISS) effect—an empirical phenomenon revealing a strong interaction between electron spin and molecular chirality, even at room temperature [17–19]. The strong spin-chirality coupling due to CISS [20, 21] allows for achiral magnetic minerals to function as chiral reagents for chemical reactions, which can be controlled by electron spin [22–24]. Although various independent measurements confirm CISS-related effects, a complete microscopic understanding of CISS remains an ongoing challenge [25]. Notably, recent theoretical work by Fransson emphasizes the role of electron correlations in explaining the high levels of spin-polarization observed in experiments [26].

Additionally, the effect of temperature on CISS through electron-phonon interactions presents an intriguing complexity [19, 27, 28], with experimental results showing trends that appear incompatible with each other [29–32]. This complexity is partly due to the fact that temperature also affects the material and molecular properties involved, complicating efforts to isolate the CISS component of the observed effects. Moreover, as our previous findings indicate that spin-chirality interactions may play a role in life’s homochirality in natural settings, we must consider temperature as an environmental variable given its significant variability in natural environments (Figure 1d). To address these challenges, we examined the temperature dependence of chirality-induced avalanche magnetization in chiral RAO crystals on magnetic surfaces stable within our temperature range, as well as the effect of temperature on the prebiotic synthesis of RAO.

Contrary to classical intuition about spin-controlled processes (Figure 1d), our findings demonstrate that the net magnetization induced by chiral molecules due to CISS, through their spin-specific interactions with the magnetic surface, significantly increases with rising temperatures (Figure 2 and Figure 3). This supports a vibronic contribution to CISS, indicating that phonon-assisted couplings play a significant role in the observed spin polarizations due to the CISS effect [28]. These findings shed light on the temperature dependence of CISS, which remains an active area of research with seemingly incompatible findings. Commensurable with these, we observed a corresponding increase in the relative yield of RAO during its prebiotic synthesis as temperature rises (Figure 4). Our results, therefore, reveal the effect of an essential component of CISS, temperature, with important implications for life’s homochirality—suggesting that spin-controlled processes contributing to RNA’s homochirality via CISS can robustly occur across a range of conditions likely

present in natural environments.

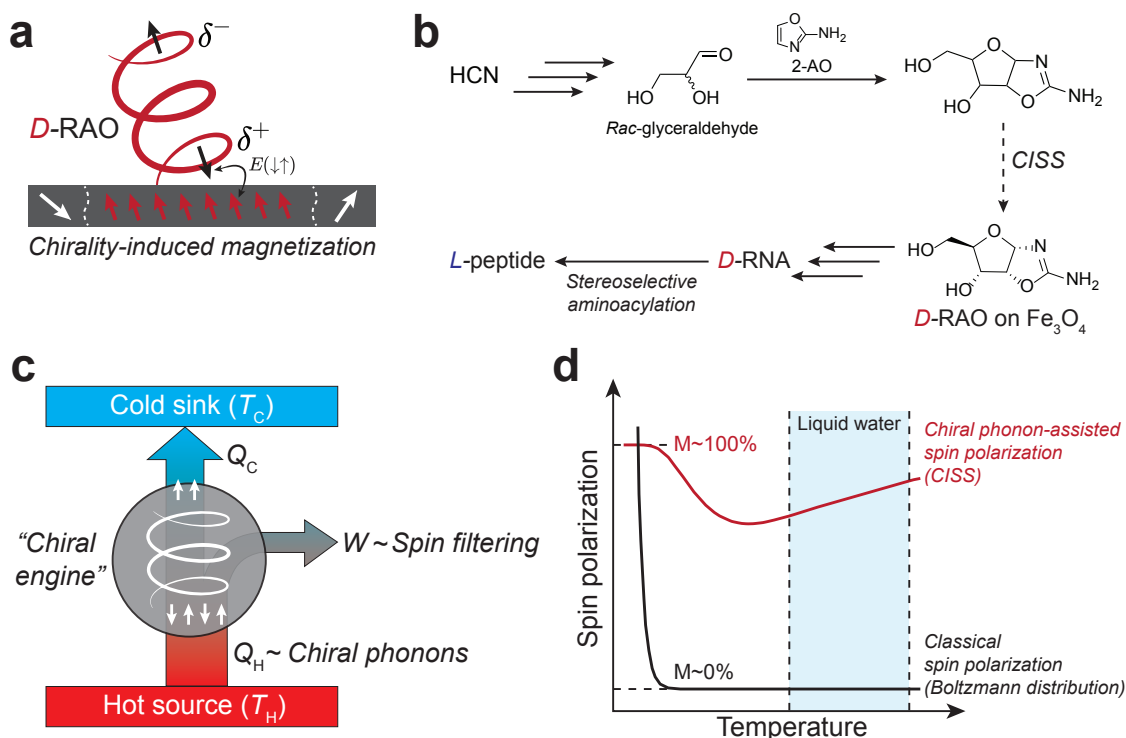


Figure 1. **a** Chiral molecules can spin-polarize magnetic surfaces through spin-exchange interactions, arising from transient spin splitting in a chiral potential due to the chirality-induced spin selectivity (CISS) effect. This induced magnetization increases in strength at higher temperatures. **b** Ribose-aminooxazoline (RAO) is a central prebiotic compound in cyanosulfidic chemistry and a precursor to RNA. Homochiral crystals of RAO can be obtained through its spin-controlled crystallization on a magnetized magnetite (Fe_3O_4) surface. The homochirality attained in RAO can then propagate to RNA and subsequently to peptides by stereoselective coded peptide synthesis, establishing RAO as a central compound in life's homochirality. **c** The temperature dependence of CISS can be interpreted with a thermodynamic picture. In this model, the work done by chiral molecules—reducing entropy by filtering accessible spin states—is compensated by heat supplied to the molecules in the form of phonons, thereby enhancing the efficiency of this “chiral engine.” **d** Schematic illustration comparing the spin polarizations predicted by a classical spin distribution to those arising from CISS. CISS provides significantly higher spin polarizations than would be observed in a classical system, particularly within temperature ranges relevant to natural environments (shaded blue region). While the Boltzmann distribution of spin states predicts an exponential decrease in polarization with increasing temperature, the phonon-electron interactions that drive CISS enhance as temperature rises.

Chiral molecules resemble Carnot engines

How can we account for the increased effectiveness of CISS with temperature without involving microscopic details? We will start with a general thermodynamic picture and incorporate microscopic analyses in the discussions.

CISS relates to the spin-filtering of electrons, meaning that chiral molecules reduce entropy by decreasing the number of available microstates of the electronic spin distribution in the microcanonical ensemble. In this framework, temperature is a derived quantity that is inversely proportional to the change in entropy. The system of interest can be considered as the electronic spin distribution of the surface molecules and the interface. According to the first law of thermodynamics, the internal energy of an isolated system remains constant. Therefore, any work done by the system must be supplied as heat entering the system. Chiral molecules perform work by filtering spin, and we can think of them as chiral molecular Carnot engines or “chiral engines”, as illustrated in (Figure 1c). To balance the work performed, these systems must absorb heat from their surroundings. Thus, chiral engines operate more effectively when heat is provided.

This thermodynamic picture is an intuitive way of visualizing the temperature dependence of CISS. However, the effect itself is a complex phenomenon involving spin-orbit coupling, electron correlations, and electron spin-phonon interactions. Fransson investigated the role of phonons and vibronic interactions in CISS, constructing a microscopic theory of CISS beyond the Born–Oppenheimer approximation—elucidating the exchange of angular momentum as electrons traverse a helical trajectory [28, 33]. This model is introduced in our discussions and will be elaborated upon in a forthcoming work by Fransson et al. Our experimental results align with this microscopic framework, indicating that phonon-chirality couplings, amplified by temperature, play an essential role in CISS.

Results

Temperature dependence of chirality-induced magnetization

We studied the effect of temperature on chirality-induced magnetization using a magneto-optical Kerr effect (MOKE) microscope and a Hall device. Both measurements showed an increase in the chirality-induced magnetization with increasing temperatures.

MOKE measurements

MOKE microscopy is an optical technique used to measure the surface magnetization of a material by reflecting polarized light from its surface, producing image contrast that is directly proportional to the relative magnetization [10, 11, 34]. MOKE microscopy was used to measure the chirality-induced avalanche magnetization on a ferromagnetic surface by enantiopure RAO crystals.

Enantiopure RAO crystals were formed on a Si/Ni(50 nm)/Au(5 nm) thin film by drop-casting an RAO water solution, as illustrated in Figure 2a. A commercial Evico-Magnetics GmbH Magneto-optical Kerr effect (MOKE) microscope, equipped with an electromagnet oriented parallel to the sample surface, was used to image the local magnetic effects induced by the enantiopure RAO crystals. The MOKE microscope provides qualitative imaging of surface magnetization by detecting the Kerr rotation, which reflects the change in the linear polarization of light as a function of the local magnetization (Figure 2a). The contrast in the MOKE images corresponds to regions with different magnetization directions relative to the incident light, allowing us to assess the influence of the enantiopure RAO crystals on adjacent magnetic domains.

Surface magnetization images of the Ni film around the enantiopure RAO crystals at different magnetic fields and temperatures (20°C blue, 40°C light blue, 60°C light red, 80°C red) were taken. Magnetic hysteresis loops were obtained from surface magnetization images by sweeping the magnetic field and averaging the intensity in areas far (Figure 2b top) and under (Figure 2b bottom) from the enantiopure RAO crystals within the same image. As the temperature increases, the magnetic hysteresis loops under the crystals widen, indicating an increase in the coercive field. In contrast, the coercive field of the bare magnetic surface far from the crystals remains constant across all temperatures. During the measurements, RAO crystals remain stable at all temperatures.

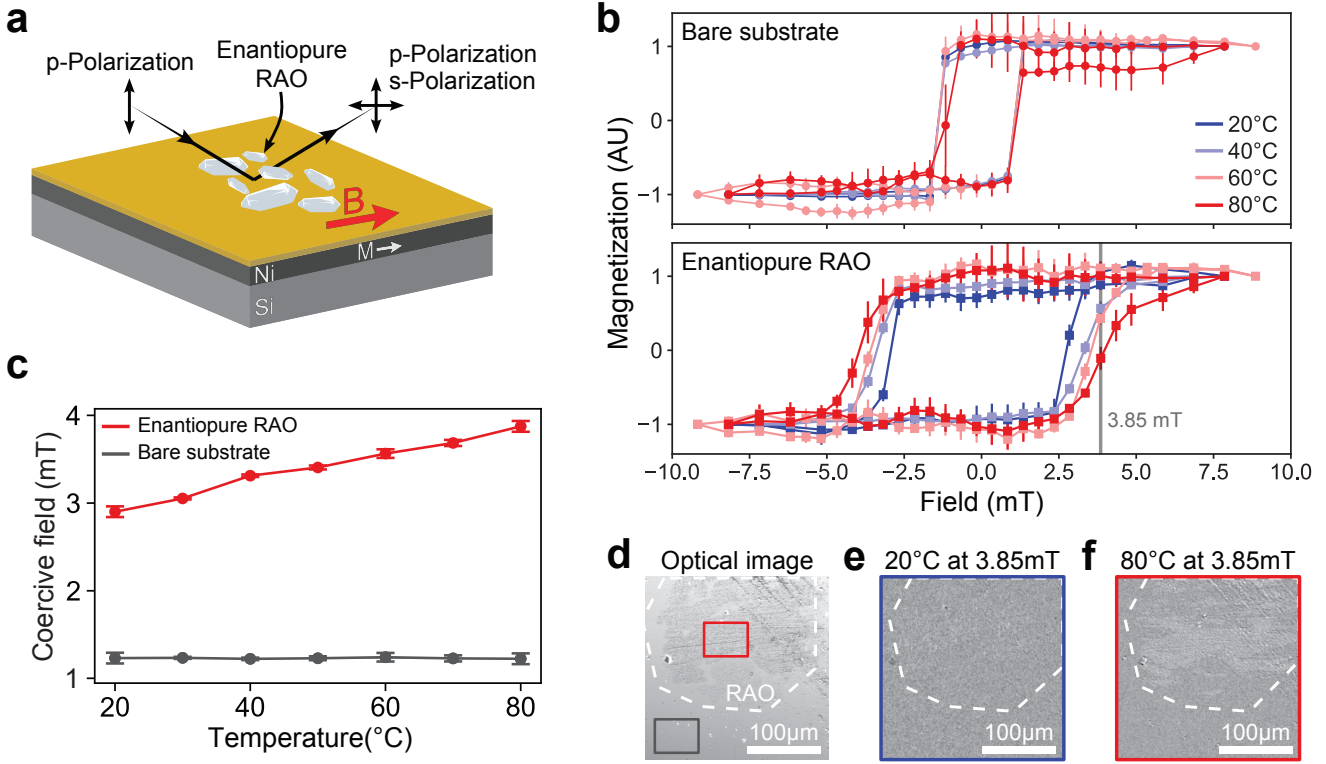


Figure 2. **a** Enantiopure RAO crystals were drop-cast onto a Si/Ni(50 nm)/Au(5 nm) thin film, forming a sample imaged with a MOKE microscope. In this setup, linearly polarized light is used to image the surface magnetization of the sample. The rotation of the polarization of the incident light corresponds to the surface magnetization. **b** Magnetic hysteresis loops are obtained by sweeping the magnetic field and averaging the intensity of regions far from (top) and under (bottom) the RAO crystals. As temperature increases, the loops under the crystals widen, indicating an increased coercive field, while the bare surface's coercive field remains constant. The vertical line at 3.85 mT is chosen to illustrate the difference in magnetization at different temperature points, as seen in panels **e** and **f**. **c** Coercive fields as a function of temperature for regions under (red) and far from (gray) the RAO crystals. The coercive field under the crystals is 2 mT higher at room temperature and increases linearly with rising temperature. **d** Optical image of the sample. The RAO crystal area is outlined with a dashed white line, and regions under the crystals and far from the crystals, where magnetization loops were taken, are marked in red/gray correspondingly. **e** Magnetic image at 20°C and a 3.85 mT magnetic field, showing all domains flipped. **f** Magnetic image at 80°C and a 3.85 mT magnetic field, where some domains under the crystals remain unflipped.

Starting with a negative field that saturates the sample, a uniform dark magnetization is observed, corresponding to -1 magnetization. As the magnetic field increases, the Ni magnetization flips to bright (+1 magnetization) at 1 mT; however, it requires an additional 2 mT to flip the domains surrounding the RAO crystals. When sweeping the field back down, the domains far from the crystals flip at -1 mT, while those under the crystals flip at -3 mT. The coercive field is plotted as a function of temperature in Figure 2c for regions under (red) and far (gray) from the crystals. The coercive field under the crystal is 2 mT higher than that of the bare surface far from the crystals and increases linearly with temperature.

The optical image of the sample is shown in Figure 2d with the area of the crystals marked in a dashed white line. The areas under the crystals (red) or far from the crystals (gray) from which the magnetization loops were taken are marked on the image. Corresponding magnetic images at a 3.85 mT magnetic field are shown in Figure 2e (20°C) and Figure 2f (80°C). In this field, all the domains flipped at 20°C while at 80°C some light domains are left under the crystals.

At higher temperatures, a more gradual transition from one magnetization to the other under the crystals is seen by the increasingly slow transition toward magnetic saturation in the magnetic hysteresis loops in Figure 2b. This is due to the smaller domain size at higher temperatures.

Thus, while stronger magnetization is observed at higher temperatures, the spread of avalanche magnetization decreases, as seen in Figure S6.

Hall effect measurements

When an electric current flows through a conductor in a perpendicular magnetic field, the Lorentz force creates a transverse Hall voltage (V_H). In ferromagnets, the anomalous Hall effect introduces an additional term from intrinsic magnetization. The total Hall voltage is: $V_H = R_0B + R_sM$. Where R_0B is the regular Hall term and R_sM is the anomalous term due to the material's magnetization. The anomalous Hall effect is commonly used to probe surface magnetization induced by chiral molecules [35, 36].

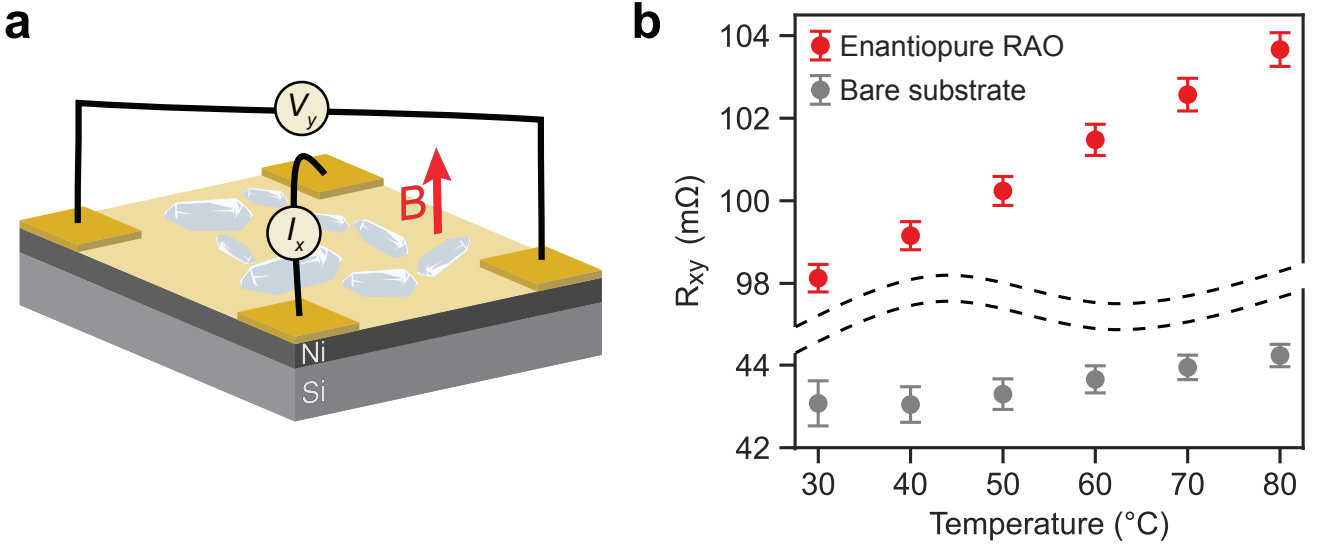


Figure 3. **a** Using Van der Pauw configuration, Hall voltage (V_y) was measured perpendicular to applied current (I_x) on a Ni/Au substrate with and without RAO crystals. All under an external magnetic field of -25 mT. **b** The temperature-dependent change in Hall resistance (R_{xy}) with (red) and without (gray) the crystals. The change in Hall resistance increases with temperature when RAO crystals are present. R_{xy} is significantly larger in the presence of RAO.

The magnetization induced by the RAO crystals on a Si/Ni(40 nm)/Au(10 nm) thin film was measured by a simple hall device in Van der Pauw configuration as shown in Figure 3a. Au pads were fabricated at the corners of a Si/Ni(40 nm)/Au(10 nm) thin film, the current was applied (I_x), and the perpendicular Hall voltage (V_y) was measured under external magnetic field of -25 mT perpendicular to the surface. Enantiopure RAO was drop-cast onto the substrate and left to dry. The Hall voltage was measured before and after RAO adsorption to avoid any variations between geometry or magnetic properties between samples.

The Hall resistance (R_{xy}) was extracted by plotting the Hall voltage as a function of the current and determining the slope from a linear fit to the data. This was calculated at different temperatures, both with and without RAO crystals. In both cases, ΔR_{xy} increases with temperature, but with the RAO crystals it increases much faster. The hall voltage in ferromagnets has contributions from both the external magnetic field and the magnetization. Therefore, at a given magnetic field, the increase in R_{xy} corresponds to increasing magnetization. The slight increase in R_{xy} of the bare substrate was observed before and contributed to the temperature dependence of the intrinsic anomalous Hall effect [37, 38].

The results indicate that the magnetization of the surface increases with temperature in the presence of chiral RAO crystals, consistent with what was observed in the MOKE results. In

Figure 3b, R_{xy} of the bare substrate, at 30°C, is $43.07 \pm 0.54(k\Omega)$ while R_{xy} of the substrate with the RAO crystals is $98.12 \pm 0.33(k\Omega)$. The $55.05(m\Omega)$ increase supports the previously established assumption that the chiral molecules themselves are magnetizing the surface.

The role of temperature in RAO synthesis

The spin-controlled processes responsible for the chirality-induced magnetization by RAO become significantly more effective at higher temperatures.

Additionally, we studied the influence of temperature on the prebiotic synthesis of RAO within a mixture of pentose-aminoxazolines, isomers of RAO. NMR measurements revealed that higher temperatures led to increased relative yields of RAO, due to its greater thermodynamic stability.

NMR measurements

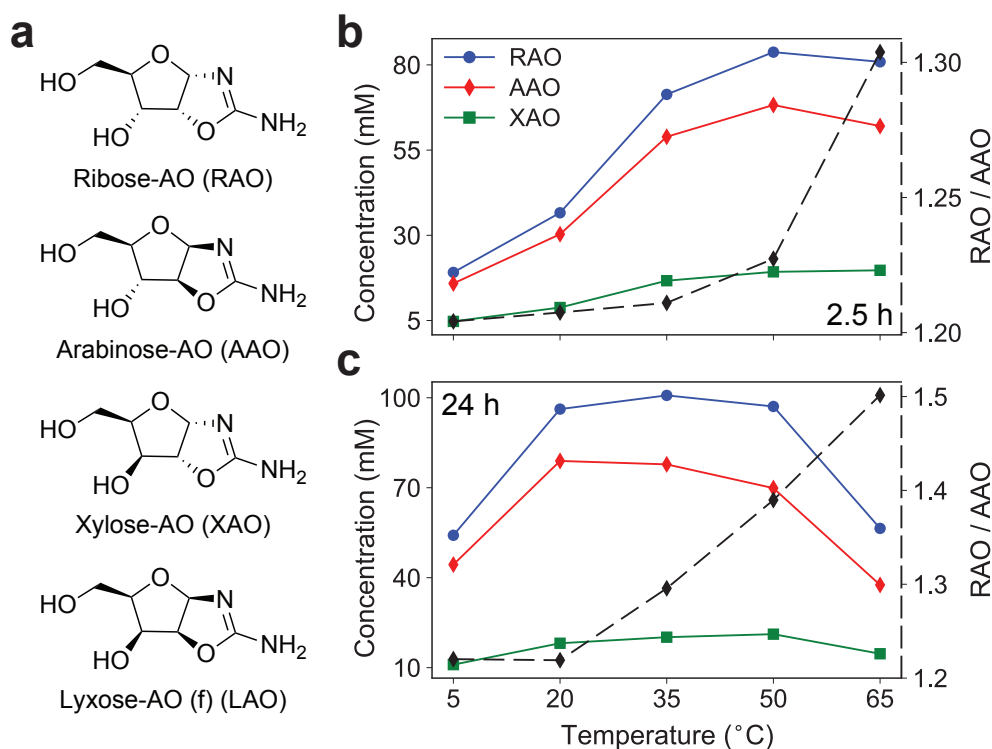


Figure 4. **a** The prebiotic synthesis of pentose-aminoxazolines produces four pairs of stereoisomers: ribose-, arabinose-, xylose-, and lyxose-aminoxazolines. While the natural ribose form is the major product, it is produced within a mixture. The arabinose form is nearly as abundant as RAO, with a ratio of RAO to AAO around 1.2 at 20°C after a day of incubation. **b, c** Concentrations of RAO (blue dots), AAO (red diamonds), and XAO (green squares) after 2.5 hours **b** and 24 hours **c** of incubation of glyceraldehyde and 2-aminoxazole as a function of temperature. The RAO to AAO ratio (second y axis, dashed line) increases significantly as both aminooxazolines begin degrading via hydrolysis. At 65°C, after a day of incubation, the ratio increases to 1.5, marking a 23% increase compared to 20°C. Therefore, at higher temperatures, the natural isomer RAO could be enriched due to the higher thermodynamic stability of RAO.

A 1:1 mixture of *DL*-glyceraldehyde and 2-aminoxazole (2-AO), each at a concentration of 250 mM, was prepared in deionized water. The solution was then divided among five tubes, with each tube incubated at a different temperature: 5°C, 20°C, 35°C, 50°C, and 65°C. The samples were analyzed by ^1H nuclear magnetite resonance (NMR) after 2.5 hours and again after 24 hours and the absolute concentrations of compounds were determined using a quantitative NMR standard.

The prebiotic synthesis discovered by the Sutherland group produced four stereoisomers—ribose-, arabinose-, xylose-, and lyxose-aminooxazolines—along with their respective enantiomers [7] (Figure 4a). Of these, ribose-aminooxazoline (RAO), the precursor to RNA, is the least soluble and crystallizes as a conglomerate. The major isomer, RAO, was produced alongside others, with arabinose-aminooxazoline (AAO) being nearly as abundant. When the reactions were completed, the pentose-AOs had an overall yield of 95%. Notably, the ratios of AOs varied across different temperatures.

Temperature influenced the reaction in two ways: it accelerated both the synthesis of pentose-AOs and, once synthesis was complete, their degradation. After 2.5 hours, before the reaction was completed, a slight increase in the RAO to AAO ratio was observed from 1.2 to 1.3 (Figure 4b). After 24 hours, when the reaction was completed for temperatures 20°C above, degradation of pentose-AO by hydrolysis to their corresponding oxazolidinones was observed. Interestingly, this degradation led to an increase in the RAO/AAO ratio from 1.2 to 1.5 from 20°C to 65°C, marking a 23% increase of the desired isomer, RAO, relative to the second most abundant isomer, AAO (Figure 4c). The observed selective degradation favoring RAO over AAO is attributed to RAO’s greater thermodynamic stability—consistent with the earlier study of isomer conversion mediated by phosphate as a catalyst [39]. Consequently, RAO’s abundance in the pentose-AO mixture increased by 14%, from 44% to 50%. Nevertheless, the RAO-to-XAO ratio decreased from 5.3 to 3.86 (Figure 4c), indicating that selective degradation by heating does not mitigate the unfavorable effects of XAO during crystallization, as observed in our previous study [9]. It is also important to note that the degradation of pentose-AOs by hydrolysis was not facilitated by a general acid-base catalyst, such as phosphate, bicarbonate or bisulfite, which could accelerate the process.

The observation that the relative abundance of the desired isomer, RAO, rises with increasing temperature complements our earlier findings on the improved efficiency of RAO-induced magnetization at higher temperatures. This confirms that our mechanism can effectively operate over a broad temperature range, demonstrating even greater efficiency at higher temperatures.

Discussion

Having provided an intuitive thermodynamic picture in the introduction, we will now present a microscopic model connecting phonons to electron spin, and thereby to magnetization. This model produces the red curve displayed in Figure 1d.

The strength of the coercive field is a measure of the axial magnetic anisotropy, which corresponds to the energy barrier stabilizing a ferromagnet against spin excitations. These spin excitations, or magnons, are essentially destructive to the ferromagnetic order. However, by studying the magnon spectrum, we gain insight into the cause of the temperature-enhanced coercive field observed in the experiments (Figure 2 and Figure 3).

The anisotropic Heisenberg model describes the magnetic excitations for a collection of interacting spin moments S_i distributed on a two-dimensional lattice at the coordinates r_i . In Hamiltonian form, this model can be written as:

$$H_H = -J \sum_{ij} \mathbf{S}_i \cdot \mathbf{S}_j - I \sum_{ij} S_i^z S_j^z \quad (1)$$

where the first term accounts for isotropic interactions between the spins, while the second provides an axial anisotropy, resulting in a preferred orientation for the total magnetic moment. The interaction parameters J and I are chosen to be positive, such that a ferromagnetic ground state is favored.

This model is capable of describing the ferromagnetic state of a local moment ferromagnet for temperatures below the Curie temperature, T_C . While the Heisenberg interaction J defines a

ferromagnetic ground state, this state is spatially isotropic, with the effect that a magnetic moment cannot be derived solely in terms of this interaction. This is also a consequence of the Mermin and Wagner theorem, which states that local isotropic interactions cannot give rise to long-range order for systems with spatial dimensions less than three [40]. The anisotropic contribution I relaxes this fundamental principle and introduces an energy gap such that any excited state of the spin system requires additional energy to be occupied—energy that may be provided by the temperature of the surrounding environment. Eventually, this energy gap is closed by the thermal energy at sufficiently high temperatures, leading to the destruction of the ferromagnetic order. This is the reason for the destruction of ferromagnetism with temperature, which is the initial decay seen in red in Figure 3d.

The unexpected increase in magnetization with temperature observed in this work can be explained by the coupling between nuclear vibrations and the localized spin moment [41]. This is the origin of the enhanced chirality-induced magnetization with increasing temperatures.

This interaction is captured by the addition of

$$H_{SQ} = - \sum_{ij} \mathbf{S}_i \cdot \mathbb{A}_{ij} \cdot \mathbf{Q}_j \quad (2)$$

where Q_i denotes the spatial displacement of the nucleus at r_i , while \mathbb{A}_{ij} represents a coupling between the localized spin moment at S_i and the displacement Q_j (or the nucleus at r_j). The nuclear displacements result in a field acting on the localized spin moments, resembling that of a magnetic field; hence, we may refer to it as a pseudo-magnetic field. It should be noted that \mathbb{A}_{ij} is a tensorial interaction with the form of a susceptibility, which arises from charge-spin fluctuations in the compound. While this susceptibility can be considered negligible in inversion-symmetric crystal structures, \mathbb{A}_{ij} is non-vanishing in chiral structures [42], where inversion symmetry is broken by definition. Introducing this component to the model is relevant in the current context, where we have chiral molecules adsorbed on a magnetite surface.

As we are interested in the effect of the spin-lattice coupling on the magnetic anisotropy, we consider the linear spin wave spectrum that results from the introduced model. The details will be presented in a follow-up work, and here, we merely present the salient features from this investigation.

In the absence of spin-lattice coupling, at lower temperatures, the linear spin wave spectrum in the limit of long wavelength is captured by the energy dispersion relation $E_q = \alpha q^2 + \beta$, where q is the reciprocal of the wavelength, $\alpha > 0$ is related to the exchange energy J , and $\beta > 0$ represents the anisotropic energy in terms of I . Therefore, the physics of the composed system is dominated by processes that are very well captured within this theoretical picture.

At higher temperatures, the dominant processes that govern the physics are related to the spin-lattice coupling, such that the energy dispersion relation must be replaced by $E_q(T) = \alpha q^2 + \beta + \gamma T$, where the additional anisotropic contribution γ provides a linear temperature dependence of the energy dispersion, as seen in the shaded blue area of the red curve in Figure 1d. The effect of this linear contribution to the anisotropy energy leads to an increase in the coercive field with temperature, in agreement with the experimental observations (Figure 2 and Figure 3). Physically, we interpret this addition to the anisotropic energy as a new channel that diverts the energy away from exciting spin waves in the system and instead generates lattice vibrations. This term is connected to heat supplied to the chiral engine, as we explained in the thermodynamic picture.

The combination of these two terms—one being destructive and the other constructive to the thermodynamic order—stabilizes the system of chiral molecules on a magnetic surface against environmental fluctuations. This provides persistent magnetization necessary for observing spin-controlled asymmetric processes due to CISS in natural environments. This inherent stability of our mechanism, together with RAO’s superior thermodynamic stability (Figure 4), enhances our scenario’s environmental plausibility.

Conclusion

Our findings show that spin-controlled asymmetric processes due to the CISS effect can promote RNA homochirality through the crystallization of a central RNA precursor, RAO, on magnetite (Fe_3O_4) surfaces. Contrary to classical expectations, temperature—an important environmental variable—actually enhances this process. Our experiments reveal that both chirality-induced magnetization by RAO and its prebiotic synthesis become more efficient as the temperature increases. These results not only provide insights into the temperature dependence of CISS, an active area of research, but also reinforce the stability of spin-controlled mechanisms involving CISS across various environmental conditions. The inherent stability of CISS, which distinguishes it from classical spin phenomena, arises from spin-phonon couplings, which appear to be crucial for the high degree of spin polarization observed in CISS experiments. Thus, our results offer both a deeper understanding of CISS and highlight its significance in the context of RNA homochirality.

Acknowledgments

We thank John Sutherland for his help in interpreting the NMR spectra and Ziwei Liu for his suggestions on quantitative NMR analysis. We thank Naama Goren from the Hebrew University Applied Physics Department for her help in interpreting the Hall measurements and Maurice Saidian from the Hebrew University Nano Center for Ni/Au evaporation. Y.P. acknowledges the funding from Marie Skłodowska-Curie Actions under Horizon Europe framework program (CISSE project No. 101071886), Carl Zeiss Stiftung (HYMMS project No. P2022-03-044), and U.S Air Force (grant No. FA8655-24-1-7390). Y.K. thanks the Israel Council of Higher Education’s VTT fellowship for women in STEM. S.F.O. and D.D.S. acknowledge the Harvard Origins of Life Initiative for funding and its members for fruitful discussions. S.F.O. also acknowledges the Kavli-Laukien fellowship program and the Kavli and Laukien Foundations for generous research funding and travel support.

References

1. Sasselov, D. D., Grotzinger, J. P. & Sutherland, J. D. The origin of life as a planetary phenomenon. *Science Advances* **6**, eaax3419 (2020).
2. Joyce, G. *et al.* Chiral selection in poly (C)-directed synthesis of oligo (G). *Nature* **310**, 602–604 (1984).
3. Ozturk, S. F. *A New Spin on the Origin of Biological Homochirality* PhD thesis (2024).
4. Blackmond, D. G. The origin of biological homochirality. *cold spring harbor perspectives in biology* **11**, a032540 (2019).
5. Sallembien, Q., Bouteiller, L., Crassous, J. & Raynal, M. Possible chemical and physical scenarios towards biological homochirality. *Chemical Society Reviews* (2022).
6. Patel, B. H., Percivalle, C., Ritson, D. J., Duffy, C. D. & Sutherland, J. D. Common origins of RNA, protein and lipid precursors in a cyanosulfidic protometabolism. *Nature chemistry* **7**, 301–307 (2015).
7. Powner, M. W., Gerland, B. & Sutherland, J. D. Synthesis of activated pyrimidine ribonucleotides in prebiotically plausible conditions. *Nature* **459**, 239–242 (2009).
8. Xu, J. *et al.* Selective prebiotic formation of RNA pyrimidine and DNA purine nucleosides. *Nature* **582**, 60–66 (2020).

9. Ozturk, S. F., Liu, Z., Sutherland, J. D. & Sasselov, D. D. Origin of biological homochirality by crystallization of an RNA precursor on a magnetic surface. *Science Advances* **9**, eadg8274 (2023).
10. Ozturk, S. F. *et al.* Chirality-induced avalanche magnetization of magnetite by an RNA precursor. *Nature Communications* **14**, 6351 (2023).
11. Kapon, Y., Kammerbauer, F., Yochelis, S., Kläui, M. & Paltiel, Y. Magneto-optical imaging of magnetic-domain pinning induced by chiral molecules. *The Journal of Chemical Physics* **159** (2023).
12. Wu, L.-F., Su, M., Liu, Z., Bjork, S. J. & Sutherland, J. D. Interstrand aminoacyl transfer in a tRNA acceptor stem-overhang mimic. *Journal of the American Chemical Society* **143**, 11836–11842 (2021).
13. Roberts, S. J., Liu, Z. & Sutherland, J. D. Potentially prebiotic synthesis of aminoacyl-RNA via a bridging phosphoramidate-ester intermediate. *Journal of the American Chemical Society* **144**, 4254–4259 (2022).
14. Ozturk, S. F., Sasselov, D. D. & Sutherland, J. D. The central dogma of biological homochirality: How does chiral information propagate in a prebiotic network? *The Journal of Chemical Physics* **159**, 061102. ISSN: 0021-9606 (Aug. 2023).
15. Hurowitz, J., Grotzinger, J., Fischer, W., McLennan, S. & et al. Redox stratification of an ancient lake in Gale crater, Mars. *Science* **356**, eaah6849 (2017).
16. Ozturk, S. F. & Sasselov, D. D. On the origins of life’s homochirality: Inducing enantiomeric excess with spin-polarized electrons. *Proceedings of the National Academy of Sciences* **119**, e2204765119. <https://www.pnas.org/doi/abs/10.1073/pnas.2204765119> (2022).
17. Naaman, R. & Waldeck, D. H. Chiral-induced spin selectivity effect. *The journal of physical chemistry letters* **3**, 2178–2187 (2012).
18. Naaman, R., Paltiel, Y. & Waldeck, D. H. Chiral molecules and the electron spin. *Nature Reviews Chemistry* **3**, 250–260 (2019).
19. Bloom, B. P., Paltiel, Y., Naaman, R. & Waldeck, D. H. Chiral Induced Spin Selectivity. *Chemical Reviews* (2024).
20. Ziv, A. *et al.* AFM-Based Spin-Exchange Microscopy Using Chiral Molecules. *Advanced Materials* **31**, 1904206 (2019).
21. Safari, M. R. *et al.* Enantioselective adsorption on magnetic surfaces. *Advanced Materials* **36**, 2308666 (2024).
22. Banerjee-Ghosh, K. *et al.* Separation of enantiomers by their enantiospecific interaction with achiral magnetic substrates. *Science* **360**, 1331–1334 (2018).
23. Bloom, B. *et al.* Asymmetric reactions induced by electron spin polarization. *Physical Chemistry Chemical Physics* **22**, 21570–21582 (2020).
24. Metzger, T. S. *et al.* Dynamic Spin-Controlled Enantioselective Catalytic Chiral Reactions. *The Journal of Physical Chemistry Letters* **12**, 5469–5472 (2021).
25. Evers, F. *et al.* Theory of chirality induced spin selectivity: Progress and challenges. *Advanced Materials* **34**, 2106629 (2022).
26. Fransson, J. Chirality-induced spin selectivity: The role of electron correlations. *The journal of physical chemistry letters* **10**, 7126–7132 (2019).

27. Kim, K. *et al.* Chiral-phonon-activated spin Seebeck effect. *Nature Materials* **22**, 322–328 (2023).
28. Fransson, J. Vibrational origin of exchange splitting and” chiral-induced spin selectivity. *Physical Review B* **102**, 235416 (2020).
29. Das, T. K., Tassinari, F., Naaman, R. & Fransson, J. Temperature-dependent chiral-induced spin selectivity effect: Experiments and theory. *The Journal of Physical Chemistry C* **126**, 3257–3264 (2022).
30. Qian, Q. *et al.* Chiral molecular intercalation superlattices. *Nature* **606**, 902–908 (2022).
31. Alwan, S., Sarkar, S., Sharoni, A. & Dubi, Y. Temperature-dependence of the chirality-induced spin selectivity effect—Experiments and theory. *The Journal of Chemical Physics* **159** (2023).
32. Yang, C. *et al.* Real-time monitoring of reaction stereochemistry through single-molecule observations of chirality-induced spin selectivity. *Nature Chemistry* **15**, 972–979 (2023).
33. Fransson, J. Charge and spin dynamics and enantioselectivity in chiral molecules. *The Journal of Physical Chemistry Letters* **13**, 808–814 (2022).
34. Sharma, A. *et al.* Control of magneto-optical properties of cobalt-layers by adsorption of α -helical polyalanine self-assembled monolayers. *Journal of Materials Chemistry C* **8**, 11822–11829 (2020).
35. Kumar, A. *et al.* Chirality-induced spin polarization places symmetry constraints on biomolecular interactions. *Proceedings of the National Academy of Sciences* **114**, 2474–2478 (2017).
36. Eckshtain-Levi, M. *et al.* Cold denaturation induces inversion of dipole and spin transfer in chiral peptide monolayers. *Nature communications* **7**, 10744 (2016).
37. Ye, L., Tian, Y., Jin, X. & Xiao, D. Temperature dependence of the intrinsic anomalous Hall effect in nickel. *Phys. Rev. B* **85**, 220403. <https://link.aps.org/doi/10.1103/PhysRevB.85.220403> (22 June 2012).
38. Lavine, J. M. Extraordinary Hall-Effect Measurements on Ni, Some Ni Alloys, and Ferrites. *Phys. Rev.* **123**, 1273–1277. <https://link.aps.org/doi/10.1103/PhysRev.123.1273> (4 Aug. 1961).
39. Powner, M. W. & Sutherland, J. D. Phosphate-mediated interconversion of ribo-and arabino-configured prebiotic nucleotide intermediates. *Angewandte Chemie International Edition* **27**, 4641–4643 (2010).
40. Mermin, N. D. & Wagner, H. Absence of ferromagnetism or antiferromagnetism in one-or two-dimensional isotropic Heisenberg models. *Physical Review Letters* **17**, 1133 (1966).
41. Fransson, J. *et al.* Microscopic theory for coupled atomistic magnetization and lattice dynamics. *Physical review materials* **1**, 074404 (2017).
42. Fransson, J. Chiral phonon induced spin polarization. *Physical Review Research* **5**, L022039 (2023).

Methods

Preparation of magnetic surfaces

For the MOKE measurements, ferromagnetic Ti(8 nm)/Ni(30 nm)/Au(5 nm) surfaces were evaporated by electron beam under a high-vacuum of 3×10^{-7} Torr on silicon (100) wafer. The thin gold coating was used to prevent the oxidation of the magnetic substrate and preserve its spin-polarization properties. The surfaces were cleaned thoroughly with acetone and ethanol before every experiment.

For the Hall measurements, Ni(40 nm)/Au(10 nm) surfaces were evaporated onto a Si/SiO wafer using electron beam evaporation (VST Metals Evaporator) under pressure of 3×10^{-6} Torr. An aluminum mask was used to form four, $3 \times 3\text{mm}^2$, corner contact pads on the sample for better electrical connectivity to the surface. Ti(10 nm)/Au(50 nm) pads were evaporated under cooling conditions on top of the surface.

RAO synthesis

D- and *L*-ribo-aminooxazolines (RAO) were synthesized by the reaction of two equivalents of cyanamide (5 g, 0.12 mol) with one equivalent of the *D*- and *D*-ribose (9 g, 0.06 mol) in aqueous ammonia (3.5%, 10 mL). After the reaction, enantiopure RAO was crystallized, the solution was filtered, and the crystals were dried and ground into powder. 20 mM solutions of *D*- or *L*-RAO were prepared in pure water and used in the experiments.

RAO crystallization

For the MOKE experiments, small (around 1-10 μm) and dense crystals were obtained by drop casting 5 μL of *L/D*-RAO solution on Ti(8 nm)/Ni(30 nm)/Au(5 nm) surfaces. Samples were then placed in the fridge (-18°C) for two cycles of two hours, with a two-hour interval at room temperature. Finally, samples were dried overnight at room temperature and areas of amorphous aggregation and dense crystallization were obtained. For the hall experiments, 10 μL *D*-RAO solution was drop-cast onto the Ni(40 nm)/Au(10 nm) surface and dried overnight at room temperature.

MOKE microscopy

MOKE imaging and magnetometry were performed using a commercial Evico Magnetics GmbH magneto-optical Kerr microscope. The measurements were taken in the longitudinal configuration. An in-plane magnetic field was generated by an electromagnet obtained from the microscope supplier powered by a Kepco BOP 100-4DL power supply. For the optical imaging of substrates, 20X commercial Zeiss objective lenses were used. A piezo stage actively stabilized mechanical vibrations of the sample. Temperature was controlled by a Peltier element and was measured continuously using a Pt thermistor.

Hall measurements

Hall measurements in Van der Pauw configuration were performed on Ni(40 nm)/Au(10 nm) samples coated with *D*-RAO molecules. The measurements were conducted under a constant external magnetic field of -25 mT generated by an out-of-plane electromagnet powered by a Kepco BOP 100-4DL power supply. The current was supplied by Keysight B2901A precision source while Hall voltage was measured in parallel by Keitley 2400 SourceMeter. Temperature was controlled by a Peltier element and was measured continuously using a Pt thermistor. The current was scanned from

-1 mA to 1 mA and back and forth. These measurements were repeated 5 times for each direction and at different temperatures: 30°C, 40°C, 50°C, 60°C, 70°C, and 80°C. The Hall resistance (R_{xy}) was extracted by plotting the Hall voltage as a function of the current and determining the slope from a linear fit to the data, then averaging over different repetitions.

Quantitative NMR measurements

A 1:1 mixture of *DL*-glyceraldehyde (90 g) and 2-AO (84 g), each at 250 mM, was prepared in 4 mL of DI water. The pH was not adjusted after mixing the reagents. This solution was divided into five tubes, each containing 800 μ L of liquid, and incubated at five temperatures: 5°C, 20°C, 35°C, 50°C, and 65°C. Samples were analyzed at two time points: 2.5 hours and 24 hours.

For each NMR measurement, 300 μ L of liquid from the sample was extracted and placed in an NMR tube. The NMR tubes were immediately placed in a water ice bath to slow the reaction, ensuring that measurement time would not impact the comparison across samples. ^1H NMR spectra were measured in water with a Bruker 400 MHz NMR spectrometer, using the water suppression feature.

Quantitative NMR analyses were performed by placing a D_2O and standard mixture (99.9 atom % D, with 0.75 wt.% 3-(trimethylsilyl)propionic-2,2,3,3- d_4 acid sodium salt, or TSP- d_4), inside a thin tube inserted within the sample NMR tube. The TSP- d_4 standard in D_2O , with 9 protons in its singlet, was diluted with pure D_2O to give a singlet with 50 mM protons by assignment. The 0 ppm TSP- d_4 singlet was also used to calibrate the chemical shift of the NMR spectra. NMR analyses were conducted on the H (C1') doublets of pentose aminooxazolines, with spectrum processing and integration performed using Mnova software.

The same standard tube was reused for each NMR scan for consistency. Moreover, this method of placing the quantitative standard in a separate tube allowed for quantitative analysis without interference with the reaction mixture and prevented proton exchange with D_2O , which could have complicated integration. The concentrations of pentose-AOs were determined by integrating their doublets in the 5.4–6 ppm range.

Supporting Information

Contents

1	Methods for MOKE Measurements	16
1.1	MOKE Setup	16
1.2	Effect of RAO Chirality	16
1.3	Magnetic Field Sweep	17
1.4	Sample Stability at Higher Temperatures	18
1.5	Domain Area Analysis	18
1.6	Errors in MOKE Measurements	19
1.7	MOKE Analysis Code	20
2	Methods for Hall Measurements	22
2.1	Hall Setup	22
2.2	Analysis of Hall Measurements	22
2.3	Hall Analysis Code	24
3	Methods for NMR Measurements	24
3.1	Quantitative NMR Analysis	25

1 Methods for MOKE Measurements

1.1 MOKE Setup

MOKE measurements were taken by a commercial Evico Magnetics GmbH magneto-optical Kerr microscope equipped with an electromagnet and a piezo controller for mechanical stabilization, as seen in Fig. S1.

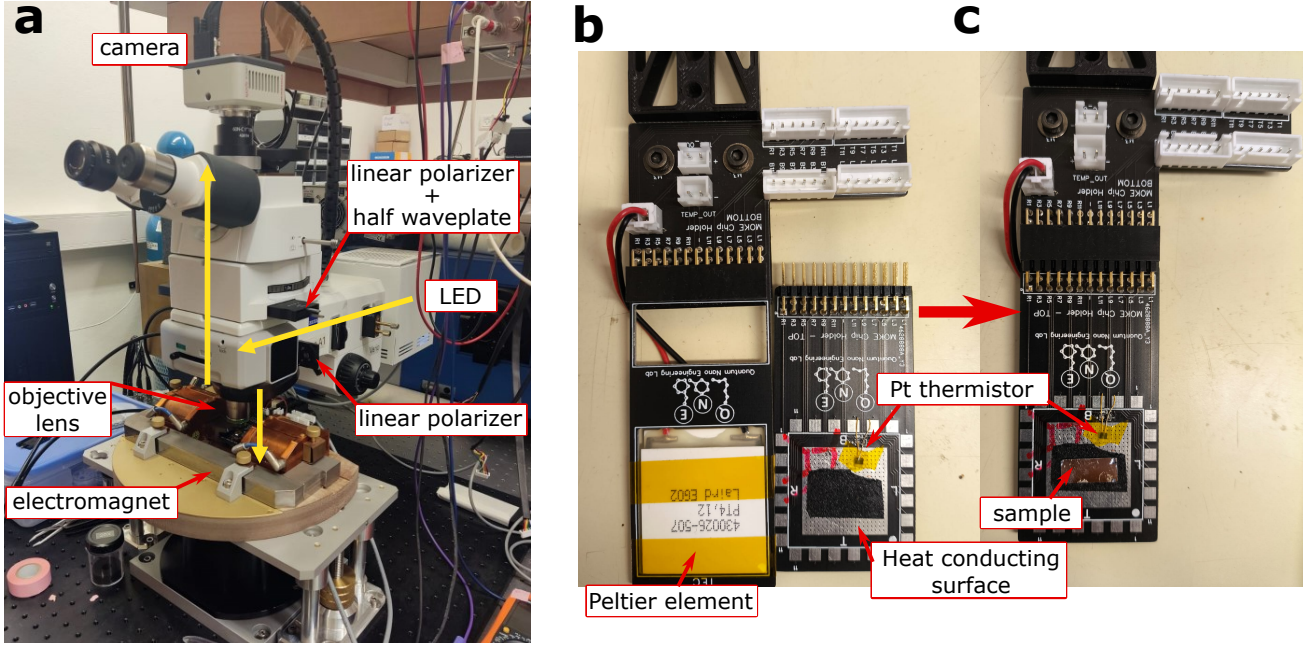


Figure S5. **a** Magneto-optical Kerr effect microscope (MOKE) setup is displayed. The magnetic surface is imaged by a Zeiss objective, and an in-plane magnetic field was generated by an electromagnet placed around the imaging plane of the microscope. The yellow arrows represent the optical path. **b** A printed circuit board (PCB) with a Peltier element for heating connected to **c** a PCB sample holder. The sample is glued to a heat-conducting surface using carbon tape with a Pt thermistor to monitor temperature.

1.2 Effect of RAO Chirality

The MOKE experiment was repeated using both L- and D-chiralities of RAO crystals. In Figure S6a, the magnetic hysteresis loops of Ni are presented for regions far from (top) and directly beneath (bottom) the D-RAO crystals. For the L-RAO sample, the magnetic properties of the bare Ni surface remained unchanged at all temperatures. In contrast, for the D-RAO sample, the coercive field of the bare Ni surface decreased at higher temperatures. Nonetheless, the difference in the coercive field between the regions beneath and far from the crystals increased with temperature, as shown in Figure S6b. In Figure S6c, this difference is compared for both L- and D-chiralities, where a similar linear trend is observed for both.

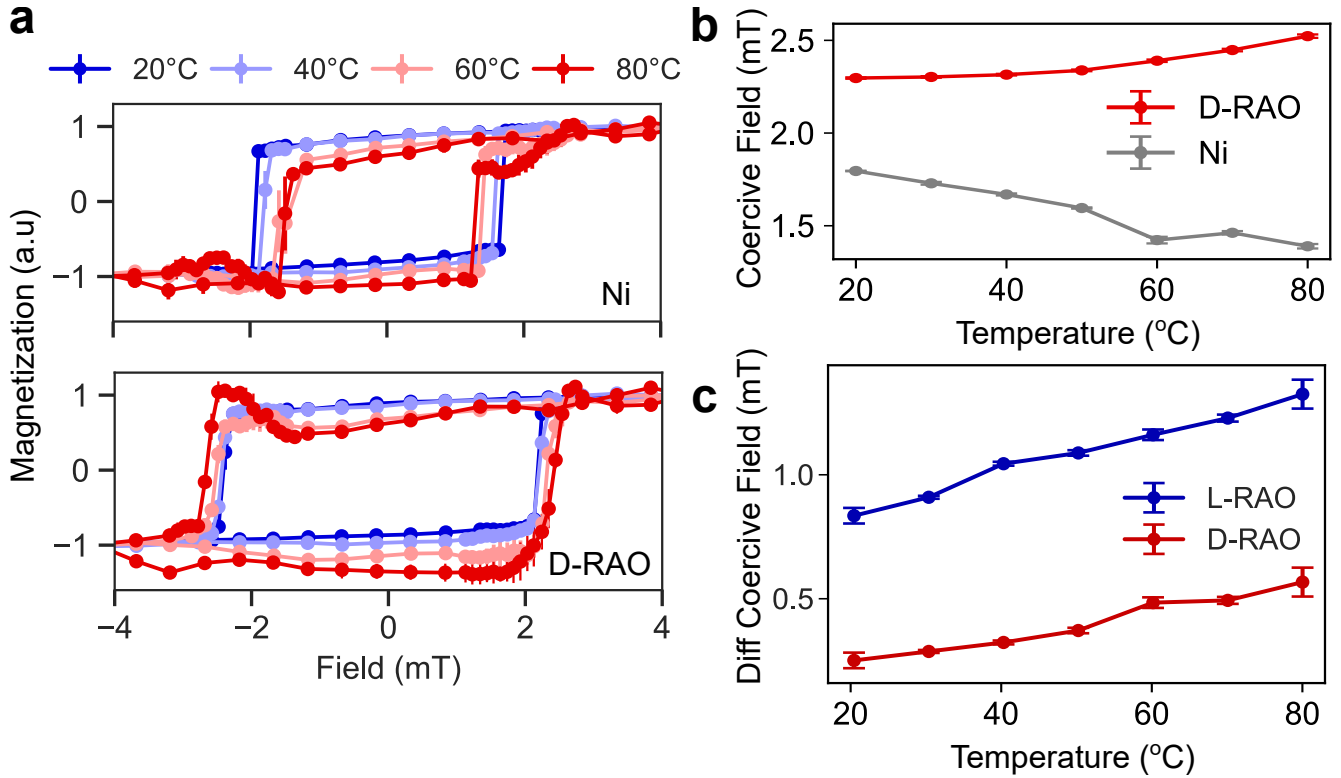


Figure S6. a Magnetic hysteresis loops of Ni with D-RAO crystals, measured far from (top) and beneath (bottom) the crystals using MOKE. b Coercive field of Ni far from (gray) and beneath the crystals (red). c Coercive field differences due to L-RAO (blue) and D-RAO (red) crystals.

1.3 Magnetic Field Sweep

Magnetic hysteresis loops of Ni were measured by sweeping the magnetic field from positive to negative and back to positive. MOKE images at various magnetic fields are shown in Figure S7. Upon reaching the coercive field of bare Ni, the domains far from the crystals flip from dark to bright. A higher demagnetization field is required to flip the domains beneath the crystals. This process is symmetric and occurs similarly when sweeping the field from negative to positive. Full hysteresis measurements at 20°C and 80°C are available in Videos S1 and S2, respectively.

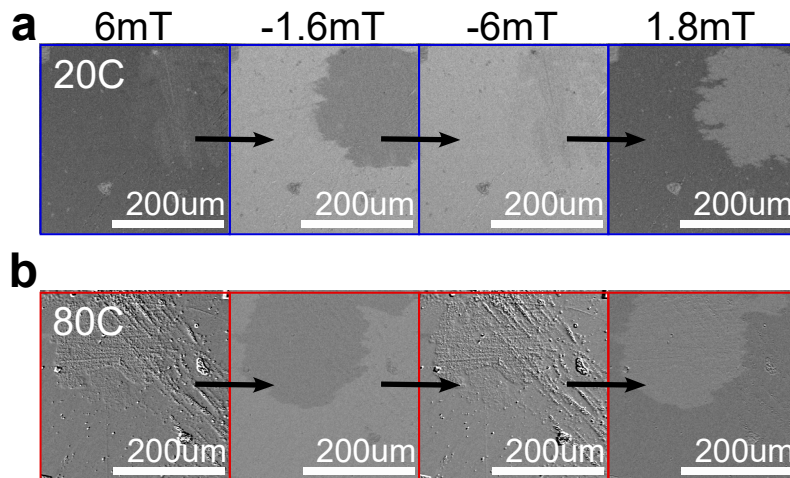


Figure S7. MOKE images at different magnetic fields at 20°C (a) and 80°C (b)

Video S1: Kerr hysteresis measurement of the Ni/Au surface with RAO crystals at 20°C. Domains around the chiral crystals have a higher magnetic coercivity, and they do not flip until a

higher demagnetizing field is applied compared to the domains far from the chiral crystals.

Video S2: Kerr hysteresis measurement of the Ni/Au surface with RAO crystals at 80C. Domains around the chiral crystals have a higher magnetic coercivity, and they do not flip until a higher demagnetizing field is applied compared to the domains far from the chiral crystals.

1.4 Sample Stability at Higher Temperatures

MOKE hysteresis measurements were repeated after several heating and cooling cycles and over a period of months. As shown in Figure S8, the magnetic properties of the sample remained unchanged. This suggests that the crystals are stable at elevated temperatures and over time. The observed local increase in the coercive field at higher temperatures in Figure 2 is therefore attributed to the coupling between nuclear vibrations and the localized spin moment, rather than any conformational changes in the molecules.

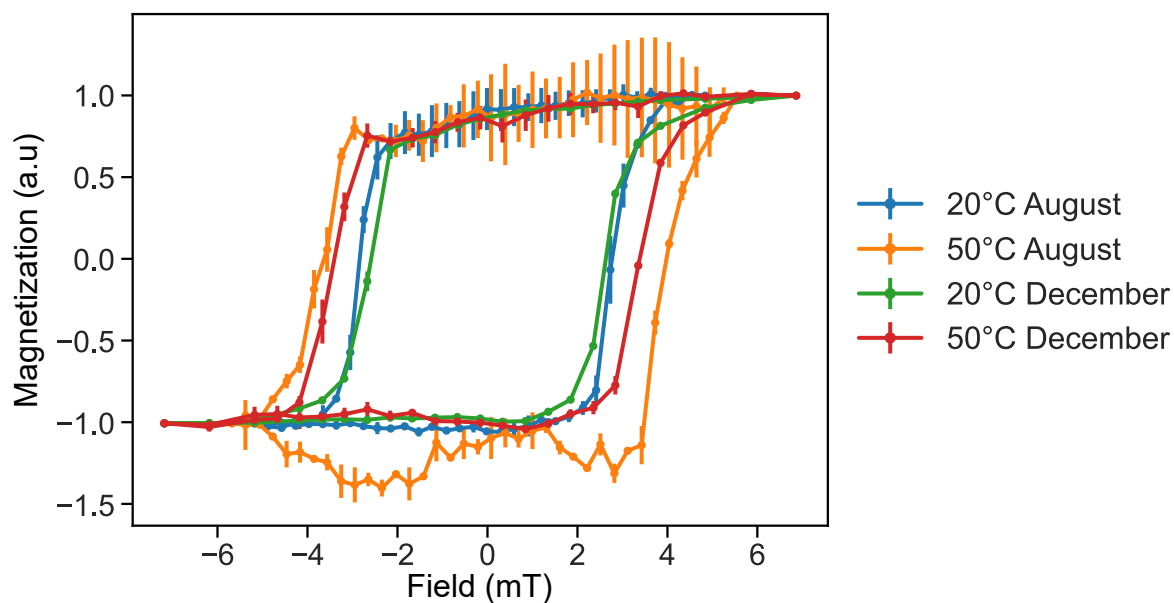


Figure S8. MOKE hysteresis loops measured in August and December after multiple heating and cooling cycles. The magnetic properties remained constant.

1.5 Domain Area Analysis

The relationship between domain size, magnetic field strength, and temperature was investigated. For each MOKE image, the flipped domain area was quantified by analyzing the intensity histogram. Once the domains began to flip, the intensity histogram displayed two Gaussian distributions corresponding to the light and dark domains. An example histogram and the associated magnetic image are shown in Figure S9. The image was binned to help differentiate between light and dark pixels and reduce noise.

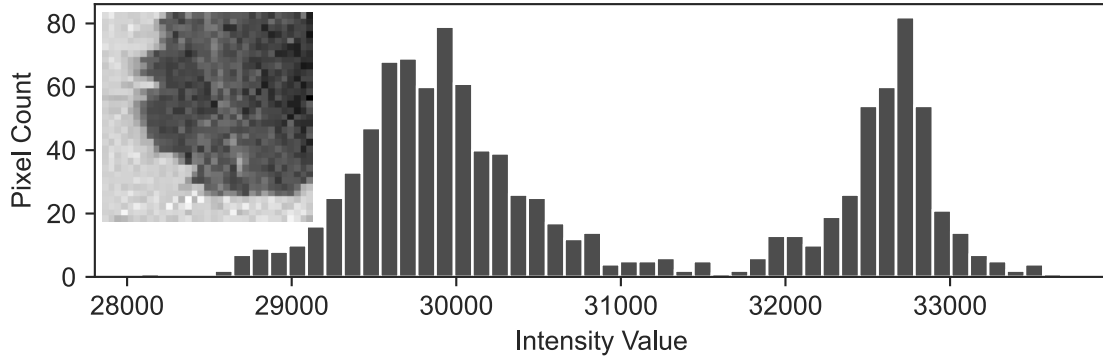


Figure S9. Intensity histogram from a MOKE image (inset), showing two Gaussian distributions for the light and dark domains.

A threshold value (e.g., 31,500 in this example) was defined between the two distributions, with pixels above the threshold classified as bright and those below classified as dark. The ratio of bright pixels to the total pixel count in the image was calculated and plotted as a function of the magnetic field for regions beneath the crystals (Figure S10a top) and far from the crystals (Figure S10a bottom).

The data were fitted using the function $A \tanh\left(\frac{x-B}{\alpha}\right) + C$, where the parameter α represents the slope of the transition. In the absence of the crystals, a smaller absolute value of α was observed, indicating a sharper transition and faster domain flipping. Figure S10b presents α as a function of temperature, comparing areas beneath and far from the crystals. At higher temperatures, smaller domain sizes resulted in slower transitions and reduced magnetization spread.

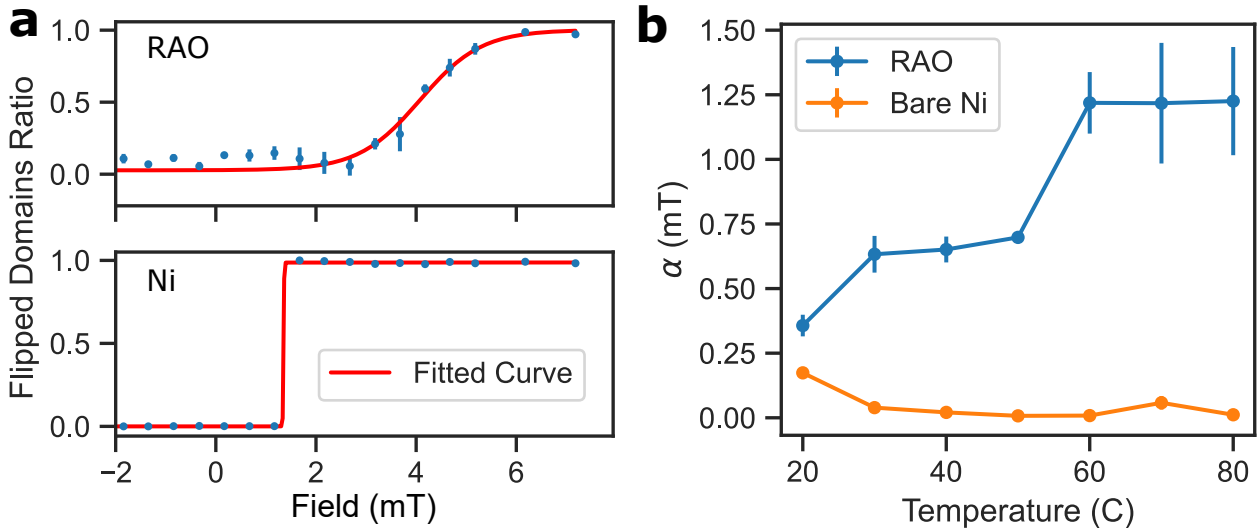


Figure S10. Relative flipped domain area as a function of magnetic field beneath the crystals (**a** top) and far from the crystals (**a** bottom). A $\tanh(x)$ fit is shown in red. **b** Fitting parameter α , representing the slope of the transition, as a function of temperature beneath (blue) and far from (orange) the crystals.

1.6 Errors in MOKE Measurements

MOKE measurements were repeated at least five times to minimize errors arising from vibrations and sample drift. Since MOKE imaging involves subtracting a magnetically saturated background image, it is particularly sensitive to movement and drift, which were more pronounced at higher temperatures. This increased instability is evident in Video S2 compared to S1. Error bars in the hysteresis loop represent a standard error of the mean ($\frac{\sigma}{\sqrt{n}}$; where σ is the standard deviation).

1.7 MOKE Analysis Code

The code used for data processing and analysis is provided below:

```
# MOKE Analysis

# Import the data:
def readfile(file, path):
    """
    Read and preprocess data from a file.
    """
    df = pd.read_csv(path + '\\\\' + file, sep='\\t')
    data = np.array(df)
    # Normalize, center, and flip the hysteresis loop
    data[:, 1] = data[:, 1] - (np.max(data[:, 1]) + np.min(data[:, 1])) / 2 #
    Center
    data[:, 1] = data[:, 1] / np.max(data[:, 1]) # Normalize
    data[:, 1] = -data[:, 1] # Flip
    return data

# Extract hysteresis loop from images
def hist_on_area(path, file, X, Y):
    """
    Extract hysteresis loop signal from images.
    """
    data = readfile(file, path)
    field = data[:, 0]
    signal = np.zeros(len(field))
    cnt = 0

    for images in sorted(os.listdir(path)):
        if images.startswith("image0"):
            im = Image.open(path + "\\\" + images)
            im_array = np.asarray(im.rotate(0)) # Rotate and convert to array
            signal[cnt] = np.sum(im_array[X[0]:X[1], Y[0]:Y[1]])
            cnt += 1

    # Correct drift and normalize
    drift = signal[-1] - signal[0]
    signal = signal - np.linspace(0, drift, num=len(signal)) # Drift correction
    signal = signal - (np.max(signal) + np.min(signal)) / 2 # Center
    signal = signal / signal[np.argmax(field)] # Normalize
    return field, signal

# Calculate coercive field width
def find_width(x, vector):
    """
    Calculate the width of the hysteresis loop.
    """
    sign_change_indices = [i for i in range(len(vector) - 1) if np.sign(vector[i])
        != np.sign(vector[i + 1])]
    x1, y1, m1, b1 = interpolate_zero(x, vector, sign_change_indices[0])
    x2, y2, m2, b2 = interpolate_zero(x, vector, sign_change_indices[1])
    return abs(-b2 / m2 - -b1 / m1)

# Helper for linear interpolation
def interpolate_zero(x, y, idx):
    y1, y2 = y[idx], y[idx + 1]
    x1, x2 = x[idx], x[idx + 1]
    m = (y2 - y1) / (x2 - x1)
    b = y1 - m * x1
```

```

    return x1, y1, m, b

# Domain Size Analysis
def bin_image(image_array, bin_size):
    """
    Reduce noise by binning the image.
    """
    height, width = image_array.shape
    cropped_array = image_array[:height // bin_size * bin_size, :width // bin_size *
        bin_size]
    shape = (height // bin_size, bin_size, width // bin_size, bin_size)
    return cropped_array.reshape(shape).mean(axis=(1, 3))

def find_ratio(full_path, X, Y, threshold, bin_size):
    """
    Calculate the ratio of bright pixels in a specified region.
    """
    im = Image.open(full_path).crop((X[0], Y[0], X[1], Y[1]))
    binned_array = bin_image(np.asarray(im), bin_size)
    bright = np.sum(binned_array > threshold)
    return bright / binned_array.size

# Sigmoidal Fitting
def sigmoidal(x, Xc, A, alpha, Yc):
    """
    Sigmoidal model based on a hyperbolic tangent function.
    """
    return A * np.tanh((x - Xc) / alpha) + Yc

def find_fit(x, y, p0=[0.1, 1, 0.01, 0.5]):
    """
    Fit data to the sigmoidal function.
    """
    params, covariance = curve_fit(sigmoidal, x, y, p0=p0)
    return params, covariance

```

2 Methods for Hall Measurements

2.1 Hall Setup

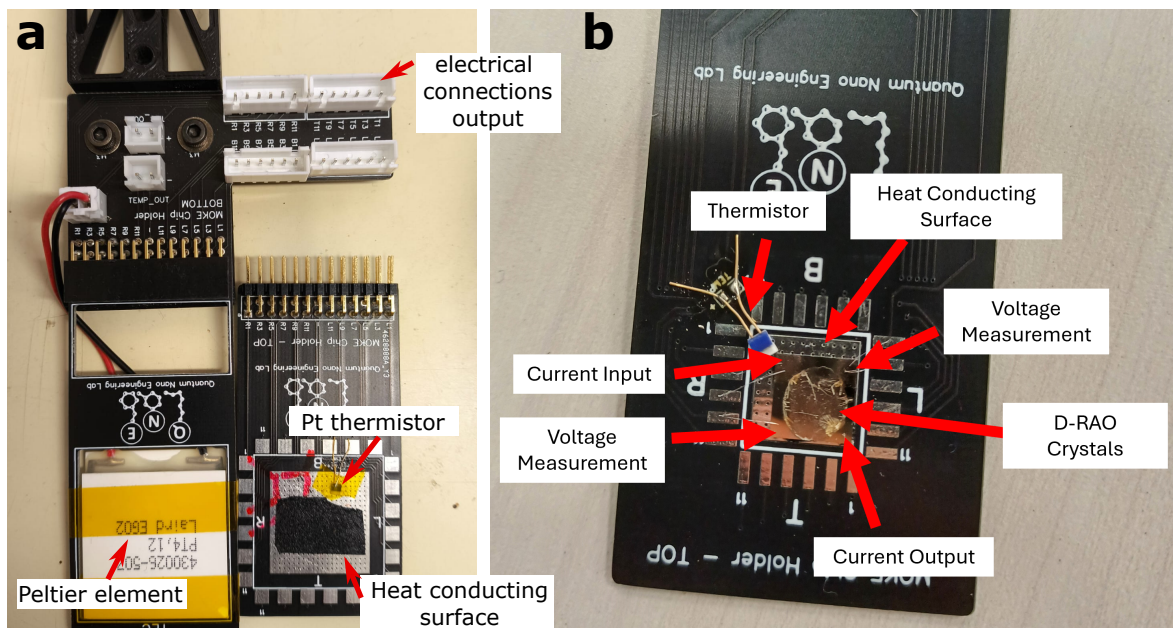


Figure S11. **a** A printed circuit board (PCB) with a Peltier element for heating connected to **b** a PCB sample holder. The Ni/Au sample is glued to a heat-conducting surface using carbon tape with a Pt thermistor to monitor temperature. Au pads are evaporated to the corners of the sample. The pads are electrically connected to the PCB sample holder by gold wires, which in turn are electrically connected within the PCB to the electrical connection output.

2.2 Analysis of Hall Measurements

The Hall Van der Pauw measurements were performed on both bare Ni and Ni samples after drop-casting RAO molecules. The measurements were conducted under varying external magnetic fields of -50 mT, -25 mT, 0 mT, 25 mT, and 50 mT. The out-of-plane magnetic field was generated by an electromagnet obtained from the MOKE microscope supplier powered by a Kepco BOP 100-4DL power supply. For each constant external field, the current was scanned from -1 mA to 1 mA in 101 steps, and the Hall voltage was measured. Each scan was repeated 5 times in the forward direction (-1 mA to 1 mA) and 5 in the reverse direction (1 mA to -1 mA). These measurements were repeated at six different temperatures: 30°C, 40°C, 50°C, 60°C, 70°C, and 80°C. A linear relationship was observed for each measurement of the Hall voltage as a function of the current. A linear function was fitted to each measurement with the slope of the fit being the hall resistance, R_{xy} . For example, the five repetitions in the forward direction of the Hall IV curve and the corresponding fits for Ni/Au with RAO crystals at 50mT and 80°C shown in Figure S12.

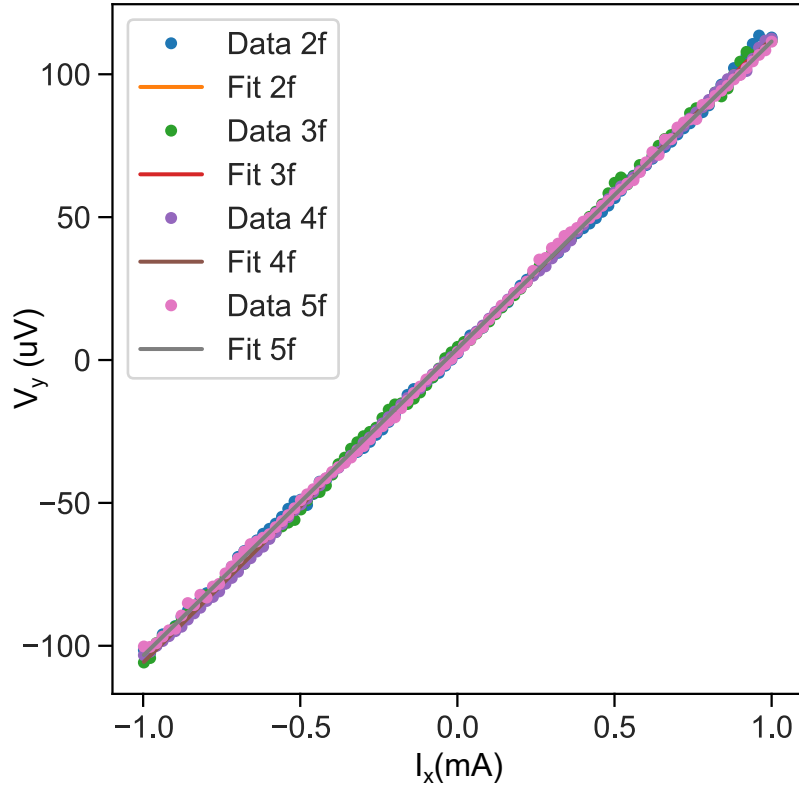


Figure S12. Hall IV curve for Ni/Au with RAO crystals at 50mT and 80°C

R_{xy} was averaged across all repetitions for each specific external field, temperature, and direction (forward or reverse), both with and without the D-RAO molecules. For each of these averages, a standard error was calculated. R_{xy} for all the temperatures and fields are represented in Figure S13.

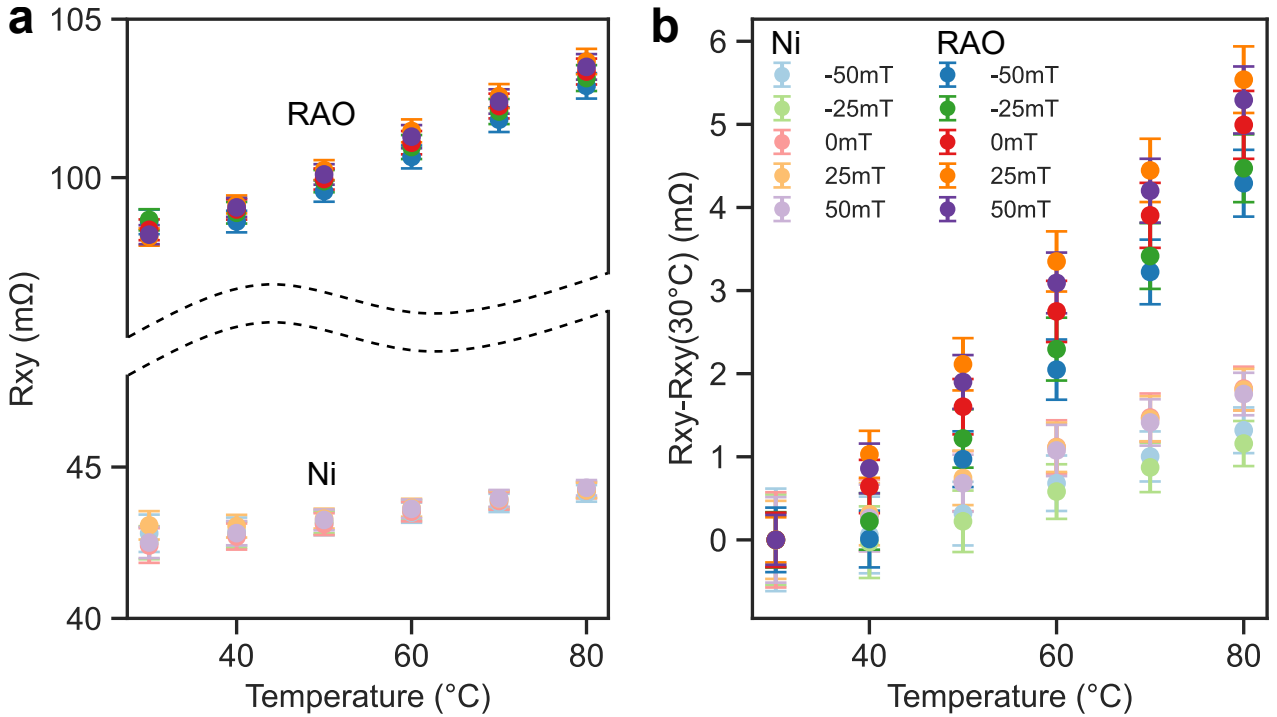


Figure S13. **a** R_{xy} for all the temperatures (30-80°C) and fields (-50 mT - blue,-25 mT - green,0 mT - red,25 mT - orange,50 mT - purple) with (dark) and without (light) RAO. **b** $R_{xy} - R_{xy}(30^\circ\text{C})$, R_{xy} value at 30°C was subtracted from the R_{xy} . In both cases, there was no significant sensitivity to the external field

As shown, the behavior is similar for all magnetic fields, even for the negative ones. We expected

to observe a negative Hall voltage for the negative fields, but this was not the case. This, along with the relatively small external fields applied (up to 50 mT), suggests that the effect we measured is the Anomalous Hall Effect, and in the applied field range, the magnetization of the Ni did not change. The -25 mT field was chosen for Figure 3 arbitrarily. R_{xy} with the molecules is much larger compared to the bare Ni without molecules and compared to the temperature effect. We, therefore, subtracted R_{xy} taken at 30°C from all data points. This way, both the D-RAO and bare substrate results start at zero, and the temperature increase can be observed as seen in Figure S13b.

2.3 Hall Analysis Code

The code used for data processing and analysis is provided below:

```
# Hall Data Analysis
def import_data_from_file(file_path):
    """
    Import Hall data starting from the marker $$$$.
    """
    marker = '$$$'
    start_row = 0
    with open(file_path, 'r') as file:
        for line_number, line in enumerate(file):
            if marker in line:
                start_row = line_number + 1
                break
    return pd.read_csv(file_path, sep='\t', skiprows=start_row)

# Organize Hall data
def divide_by_outer_loop(df, column_name):
    """
    Divide data based on unique values in the outer loop.
    """
    return {f"df_{value}": df[df[column_name] == value] for value in df[column_name].unique()}

def split_to_repetitions(df, chunk_size):
    """
    Split data into repetitions of a specified size.
    """
    return {f"{i//2+1}{'f' if i%2==0 else 'b'}": df.iloc[i:i + chunk_size] for i in range(0, len(df), chunk_size)}

def find_fit_data(xdata, ydata, init_guess, low_bound, high_bound):
    """
    Fit Hall data to a linear model.
    """
    return curve_fit(linear_fun, xdata, ydata, p0=init_guess, bounds=(low_bound, high_bound))

def linear_fun(x, a, c):
    return a * x + c
```

3 Methods for NMR Measurements

The prebiotic synthesis of pentose-aminooxazolines from glyceraldehyde and 2-aminooxazole (2-AO) yields a mixture of four stereoisomers and their corresponding enantiomers: ribose-, arabinose-, xylose-, and lyxose-aminooxazoline.

Among these, the ribose form (RAO) is the target stereoisomer, which can be obtained in enantiopure form and serves as a direct precursor to RNA pyrimidines and DNA purines. The relative abundance of RAO in the mixture increases with temperature, as determined by ^1H NMR spectroscopy in water.

Samples containing a mixture of pentose aminooxazolines in water were incubated at five temperatures (5°C , 20°C , 35°C , 50°C , and 65°C) and probed at two time intervals: 2.5 hours and 24 hours.

3.1 Quantitative NMR Analysis

NMR analyses were conducted on the H (C1') doublets of pentose aminooxazolines using a Bruker 400 MHz NMR spectrometer, with Mnova software employed for spectrum processing and integration.

For quantitative analysis, the NMR spectra were calibrated using a D_2O and standard mixture (99.9 atom % D, containing 0.75 wt.% 3-(trimethylsilyl)propionic-2,2,3,3- d_4 acid sodium salt, or TSP- d_4) placed inside a thin tube inserted into the sample NMR tube. The TSP- d_4 standard in D_2O , with 9 protons in its singlet, was diluted with pure D_2O to give a singlet with 50 mM protons by assignment.

The 0 ppm TSP- d_4 singlet was employed to calibrate the chemical shift of the NMR spectra. Following chemical shift calibration, as well as baseline and phase corrections, the NMR spectra were displayed. Figure S14 presents the complete ^1H NMR spectra measured after 2.5 hours, while Figure S16 provides the spectra obtained after 24 hours. Additionally, Figure S15 and Figure S17 offer zoomed-in views of the 5.4–6 ppm range, highlighting the H (C1') doublets of pentose aminooxazoline used for yield comparisons.

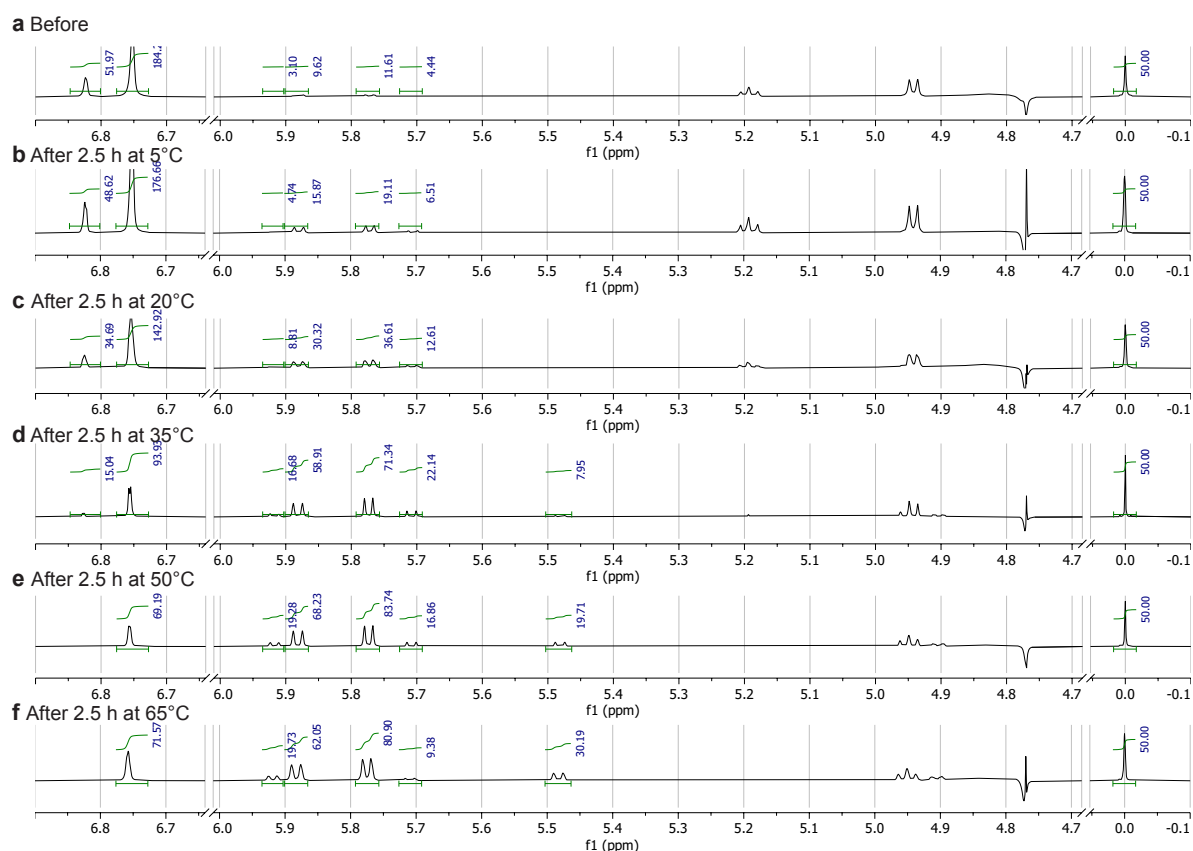


Figure S14. ^1H NMR spectra (400 MHz) after 2.5 h. **a** Spectrum obtained immediately after the reagents were mixed. **b, c, d, e, f** correspond to incubations at 5°C , 20°C , 35°C , 50°C , and 65°C , respectively.

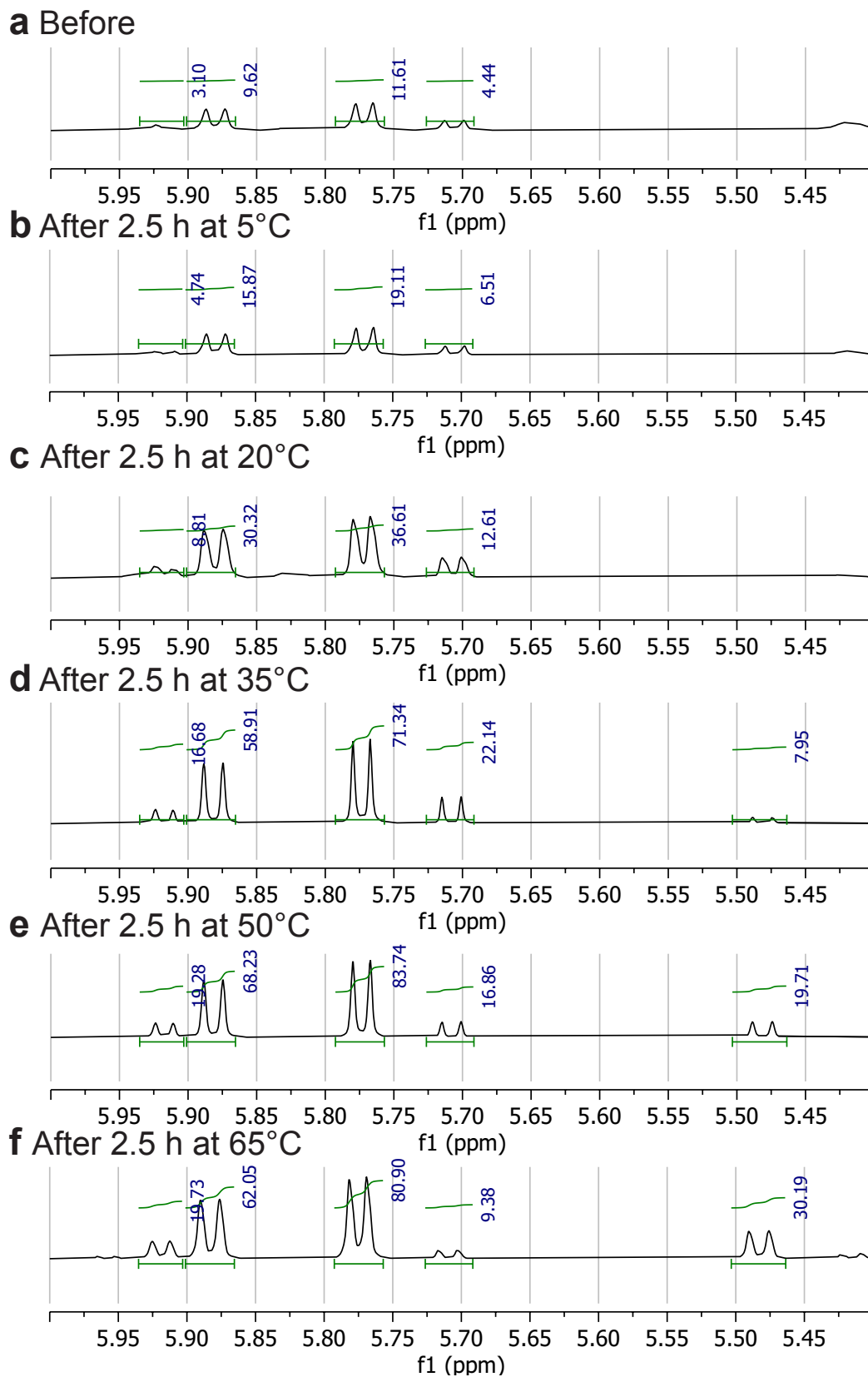


Figure S15. ^1H NMR spectra (400 MHz) after 2.5 h, zoomed into the 5.4–6 chemical shift range, highlighting the H (C1') doublets of pentose amino oxazolines. **a, b, c, d, e** correspond to incubations at 5°C, 20°C, 35°C, 50°C, and 65°C, respectively.

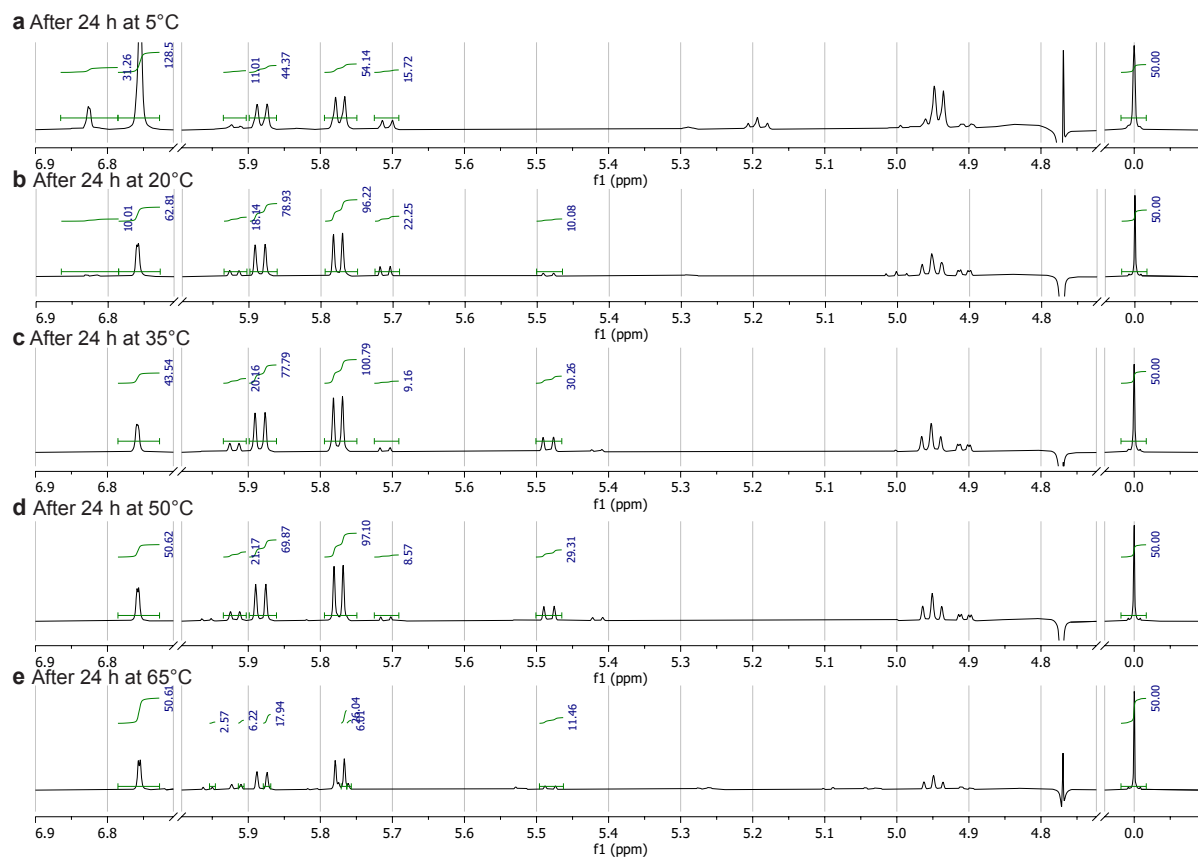


Figure S16. ^1H NMR spectra (400 MHz) after 24 h. **a, b, c, d, e** correspond to incubations at 5°C, 20°C, 35°C, 50°C, and 65°C, respectively.

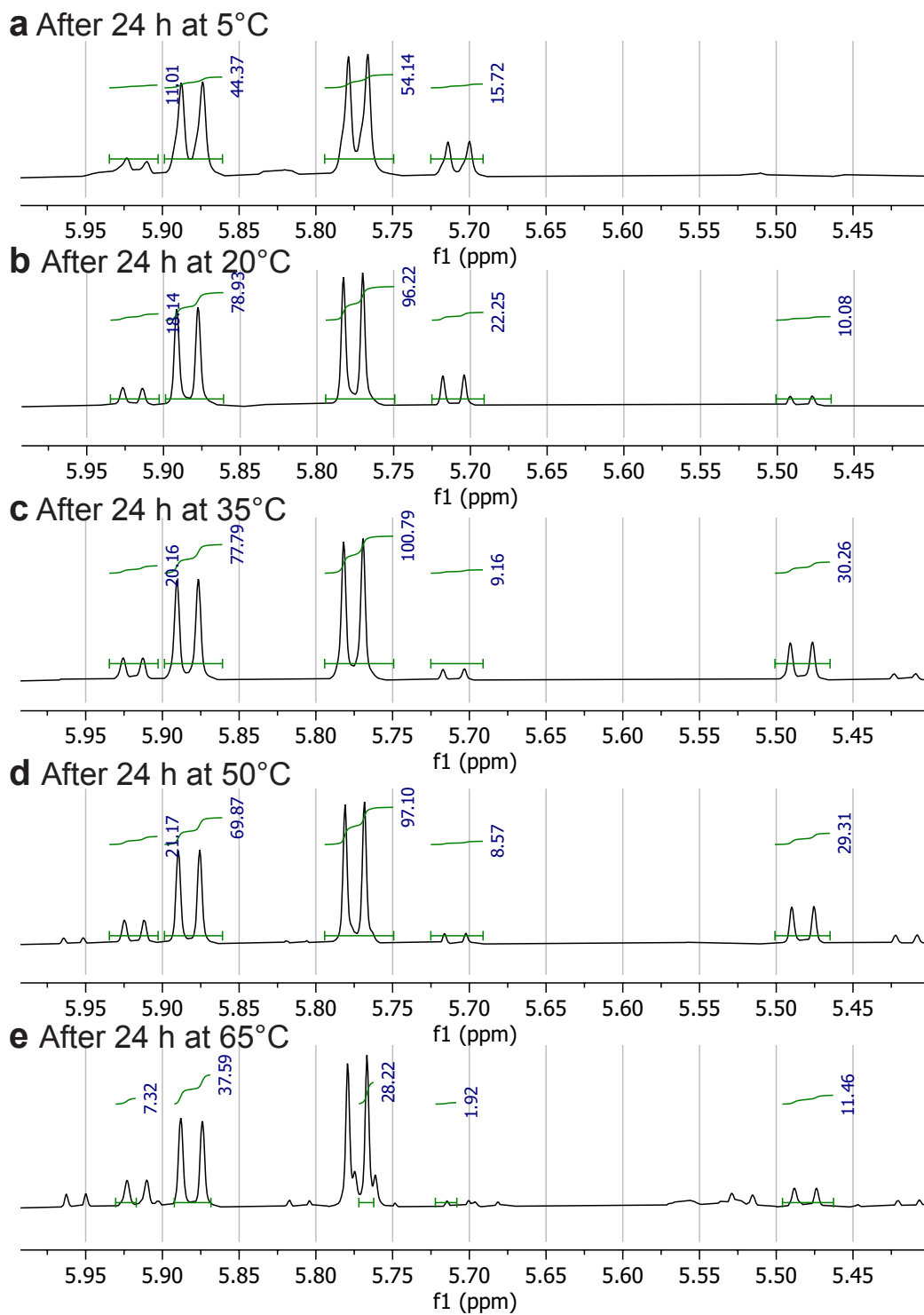


Figure S17. ^1H NMR spectra (400 MHz) after 24 h, zoomed into the 5.4–6 chemical shift range, highlighting the H (C1') doublets of pentose aminooxazolines. **a**, **b**, **c**, **d**, **e** correspond to incubations at 5°C, 20°C, 35°C, 50°C, and 65°C, respectively. In **e**, quantitative analysis was carried out by integrating a single peak of the RAO doublet to circumvent interference from the decay product signal.